Monthly Notices of the ROYAL ASTRONOMICAL SOCIETY

MNRAS **527,** 4563–4572 (2024) https://doi.org/10.1093/mnras/stad3391
Advance Access publication 2023 November 03

The black widow pulsar J1641+8049 in the optical, radio, and X-rays

A. Yu. Kirichenko ,[1,2]★ S. V. Zharikov,[1] A. V. Karpova ,[2] E. Fonseca,[3,4] D. A. Zyuzin ,[2] Yu. A. Shibanov,[2] E. A. López ,[5,6] M. R. Gilfanov,[7,8] A. Cabrera-Lavers,[9,10] S. Geier,[9,10] F. A. Dong ,[11] D. C. Good ,[12] J. W. McKee ,[13,14] B. W. Meyers,[11,15] I. H. Stairs,[11] M. A. McLaughlin [3,4] and J. K. Swiggum[16]

[1]*Instituto de Astronomía, Universidad Nacional Autónoma de México, Apdo. Postal 877, Baja California 22800, México*
[2]*Ioffe Institute, 26 Politekhnicheskaya, St. Petersburg 194021, Russia*
[3]*Department of Physics and Astronomy, West Virginia University, PO Box 6315, Morgantown, WV 26506, USA*
[4]*Center for Gravitational Waves and Cosmology, West Virginia University, Chestnut Ridge Research Building, Morgantown, WV 26505, USA*
[5]*Instituto de Física, Universidad Nacional Autónoma de México, POB 20-364, Cd.Mx. 01000, México*
[6]*Instituto de Investigación en Ciencias Físicas y Matemáticas, USAC, Ciudad Universitaria, 01012 Zona 12, Guatemala*
[7]*Space Research Institute, Russian Academy of Sciences, Profsoyuznaya 84/32, Moscow 117997, Russia*
[8]*Max-Planck-Institut für Astrophysik, Karl-Schwarzschild-Str 1, D-85741 Garching, Germany*
[9]*Instituto de Astrofísica de Canarias, Vía Láctea s/n, E-38200 La Laguna, Tenerife, Spain*
[10]*GRANTECAN, Cuesta de San José s/n, E-38712 Breña Baja, La Palma, Spain*
[11]*Department of Physics and Astronomy, University of British Columbia, 6224 Agricultural Road, Vancouver, BC V6T 1Z1, Canada*
[12]*Department of Physics and Astronomy, University of Montana, 32 Campus Drive, Missoula, MT 59812, USA*
[13]*E. A. Milne Centre for Astrophysics, University of Hull, Cottingham Road, Kingston-upon-Hull HU6 7RX, UK*
[14]*Centre of Excellence for Data Science, Artificial Intelligence and Modelling (DAIM), University of Hull, Cottingham Road, Kingston-upon-Hull HU6 7RX, UK*
[15]*International Centre for Radio Astronomy Research (ICRAR), Curtin University, Bentley, WA 6102, Australia*
[16]*Department of Physics, Lafayette College, Easton, PA 18042, USA*

Accepted 2023 October 31. Received 2023 October 26; in original form 2023 July 25

ABSTRACT

PSR J1641+8049 is a 2 ms black widow pulsar with the 2.2 h orbital period detected in the radio and γ-rays. We performed new phase-resolved multiband photometry of PSR J1641+8049 using the OSIRIS instrument at the Gran Telescopio Canarias. The obtained data were analysed together with the new radio-timing observations from the Canadian Hydrogen Intensity Mapping Experiment (CHIME), the X-ray data from the Spectrum-RG/*eROSITA* all-sky survey, and all available optical photometric observations. An updated timing solution based on CHIME data is presented, which accounts for secular and periodic modulations in pulse dispersion. The system parameters obtained through the light-curve analysis, including the distance to the source 4.6–4.8 kpc and the orbital inclination 56–59 deg, are found to be consistent with previous studies. However, the optical flux of the source at the maximum brightness phase faded by a factor of $\sim$2 as compared to previous observations. Nevertheless, the face of the J1641+8049 companion remains one of the most heated (8000–9500 K) by a pulsar among the known black widow pulsars. We also report a new estimation on the pulsar proper motion of $\approx$2 mas yr^{-1}, which yields a spin-down luminosity of $\approx$4.87 $\times$ 10^{34} erg s^{-1} and a corresponding heating efficiency of the companion by the pulsar of 0.3–0.7. The pulsar was not detected in X-rays implying its X-ray-luminosity was $\lesssim$3 $\times$ 10^{31} erg s^{-1} at the date of observations.

Key words: binaries: general – stars: neutron – pulsars: individual: PSR J1641+8049.

1 INTRODUCTION

Among about 3400 pulsars discovered to date, more than 550 belong to the class of millisecond pulsars (MSPs; Manchester et al. 2005).[1] These objects have short spin periods (P < 30 ms) and low spin-down rates ($\dot{P} \sim 10^{-20}$ to 10^{-18} s s^{-1}). The most generally accepted scenario implies that MSPs are old neutron stars (NSs) that were spun-up (or 'recycled') through angular momentum transfer by accretion from their main-sequence companions during a low-mass/intermediate-mass X-ray binary stage (Bisnovatyi-Kogan & Komberg 1974; Alpar et al. 1982). The binary MSP population comprises several classes depending on the type of the companion. In the so-called spider systems with tight orbits ($P_b \lesssim 1$ d), low-mass companions are heated and ablated by the pulsar wind of relativistic particles and radiation (e.g. Manchester 2017). Evaporated material often causes eclipses of the pulsar radio emission. Black widows (BWs), which represent a subclass of such binaries, have very low-mass ($M_c \lesssim 0.05\mathrm{M}_\odot$) almost ablated degenerate companions. The

★ E-mail: aida.taylor@gmail.com, aida@astro.unam.mx
[1]https://www.atnf.csiro.au/people/pulsar/psrcat/

Table 1. Log of the J1641 observations with GTC/OSIRIS.

Date	Filter	Exposure time (s)	Airmass	Seeing (arcsec)
12-07-2020	r'	150 × 43	1.62–1.70	0.8–1.0
13-08-2020	g'	200 × 21	1.64–1.76	0.7–1.1
13-08-2020	i'	120 × 21	1.64–1.76	0.7–0.9

origin and formation of such systems is not well understood, but it is actively discussed (Chen et al. 2013; Benvenuto, De Vito & Horvath 2014, 2015; Ablimit 2019; Ginzburg & Quataert 2021; Guo, Wang & Han 2022).

About 70 BWs have been discovered so far thanks to radio and γ-ray observations. Half of them reside in the Galactic disc (Swihart et al. 2022), while others are associated with globular clusters.[2] According to the recent census (Swihart et al. 2022), only about 20 BWs have been detected in the optical. However, optical studies allow one to determine fundamental parameters of BWs such as spectral type and temperature of a companion, irradiation efficiency, distance, as well as masses of its components when they cannot be derived from radio timing observations alone.

The binary MSP PSR J1641+8049 (hereafter J1641) was discovered in the Green Bank North Celestial Cap (GBNCC) pulsar survey (Stovall et al. 2014; Lynch et al. 2018). This is an eclipsing radio pulsar that is also presented in the list of *Fermi*-detected pulsars (Ray 2023). Its flux in the 0.1–100 GeV range is 2.0(3) × 10^{-12} erg s^{-1} cm^{-2} (Abdollahi et al. 2022). J1641 was not observed in X-rays. It has an orbital period of 2.18 h that is one of the shortest among the known BWs. The companion's minimum mass was estimated to be 0.04 $M_{\odot}$ (Lynch et al. 2018). The dispersion measure (DM) distances to the pulsar are $D_{\rm YMW16} = 3.0$ kpc and $D_{\rm NE2001} = 1.7$ kpc based on the YMW16 (Yao, Manchester & Wang 2017) and NE2001 (Cordes & Lazio 2002) models for the distribution of free electrons in the Galaxy, respectively.

Lynch et al. (2018) found a faint optical counterpart ($r = 24.0(3)$) to J1641 in the archival data, and performed photometric observations of the pulsar with the 4.3-m Lowell Discovery Telescope[3] (LDT) in the g, r, i, and z filters and with the McDonald Observatory 1 m telescope in the r' and i' filters. The counterpart revealed strong brightness variations tied to the orbital period, confirming the optical identification of the pulsar companion. Further optical studies of J1641 were recently reported by Mata Sánchez et al. (2023) who performed its phase-resolved multiband photometry with the HiPERCAM instrument at the 10.4-m Gran Telescopio Canarias (GTC) in 2019. They analysed the multiband light curves and obtained the fundamental parameters of the system, including the inclination, the Roche lobe filling factor, the companion mass, and the temperature gradient over the companion surface, as well as the distance to the system.

In this paper, we report the results of our independent phase-resolved multiband optical observations of J1641 obtained with the OSIRIS instrument at the GTC in 2020. We analyse the OSIRIS, HiPERCAM, LDT, and the 1 m telescope data of J1641 all together. In addition, we present the updated parameters of the system derived from ongoing observations with the Canadian Hydrogen Intensity Mapping Experiment (CHIME) telescope, and report an upper limit on the pulsar X-ray flux based on observations with *eROSITA* (Predehl et al. 2021) aboard the Spectrum-RG (SRG) orbital observatory (Sunyaev et al. 2021). The paper is organized as follows: observations and data reduction are described in Section 2, the radio timing analysis is presented in Section 3, while the modelling of the light curves is described in Section 4. Discussion and conclusions are given in Section 5.

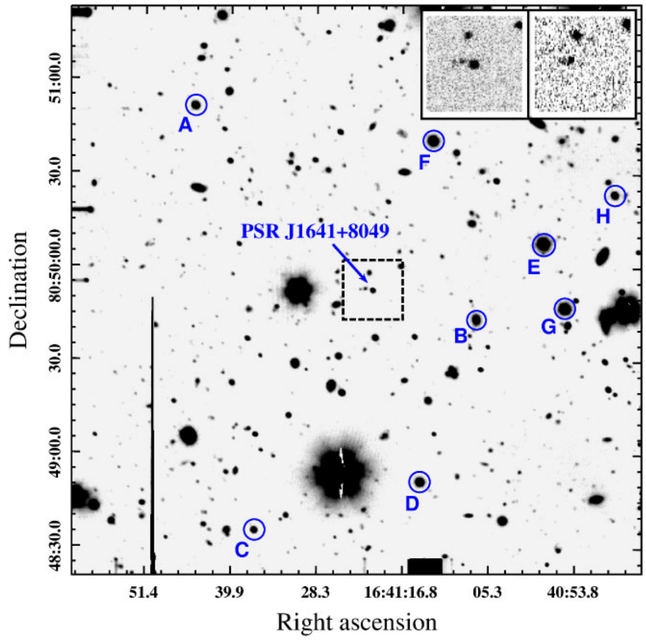

Figure 1. The 3.05 × 3.05 $arcmin^2$ J1641 FoV imaged with the GTC/OSIRIS in the r' band. The J1641 vicinity is shown by the box in the centre of the image, and the optical companion is indicated by the arrow. The left and right inserts correspond to the enlarged J1641 vicinity imaged near the companion maximum and minimum brightness phases. The stars from the Pan-STARRS catalogue listed in Table 2 and used for the photometric calibration, are marked by the capital letters.

2 OBSERVATIONS AND DATA REDUCTION

2.1 Optical data

The phase-resolved photometric observations[4] of the J1641 field were carried out during two observing runs in the Sloan g', r', and i' bands with the Optical System for Imaging and low Resolution Integrated Spectroscopy (OSIRIS) instrument at the GTC. In order to reduce the CCD readout time and increase the efficiency of the phase-resolved observations, we used windowing. The target was exposed on CCD1, and the windowed field of view (FoV) was 3.05 × 3.05 $arcmin^2$. To avoid effects from CCD defects, 5 arcsec dithering between the individual exposures was used in both observing runs. The observations roughly covered two orbital periods in total, i.e. one orbital period per each observing run. The first period was observed in the r' band only, whereas the second one was covered one month later using the alternating g' and i' bands. The log of observations is given in Table 1. The r'-band image of the pulsar field is presented in Fig. 1, where the inserts demonstrate the variability of the pulsar companion.

Using the Image Reduction and Analysis Facility (IRAF) package, we performed a standard data reduction, including bias subtraction and flat-fielding. The cosmic rays were removed from all images

[2] See https://www3.mpifr-bonn.mpg.de/staff/pfreire/GCpsr.html.
[3] Formerly known as the Discovery Channel Telescope.
[4] Proposal GTC11-20AMEX, PI A. Kirichenko

Table 2. Stars from the Pan-STARRS catalogue detected in the J1641 field and their magnitudes.

Star	g'	r'	i'
A	21.619(068)	20.575(025)	19.598(017)
B	–	21.295(137)	20.717(019)
C	–	21.316(044)	20.636(032)
D	21.142(054)	19.970(021)	18.980(011)
E	19.617(014)	18.559(009)	18.054(008)
F	20.416(030)	19.253(013)	18.683(008)
G	19.297(012)	18.744(006)	18.505(008)
H	21.403(095)	21.058(054)	19.889(012)

with the L.A.Cosmic algorithm (van Dokkum 2001). Astrometric referencing was performed using a single 180-s r'-band image and a set of stars from the Gaia DR3 catalogue (Gaia Collaboration 2023). Given the reduced image size in the windowing mode, only five field stars detected by *Gaia* appeared to be suitable for the astrometric purposes. Using these stars, we computed the astrometric solution with the formal rms uncertainties ΔRA $\lesssim$ 0.13 arcsec and ΔDec. $\lesssim$ 0.14 arcsec.

Photometric calibration was performed using the Sloan photometric standards SA111-1925 for the r' band and PG1528+062B for the g' and i' bands (Smith et al. 2002) observed during the same nights as the target. Using their instrumental magnitudes and the site extinction coefficients $k_{g'} = 0.15(2)$, $k_{r'} = 0.07(1)$, and $k_{i'} = 0.04(1)$ (Cabrera-Lavers et al. 2014), we calculated the zero points $Z_{g'} = 28.53(2)$, $Z_{r'} = 28.94(1)$, and $Z_{i'} = 28.42(1)$. To verify these zero points, we checked the sky transparency variability by comparing the instrumental magnitudes of a field star during the observations of the target. The variation did not exceed errors of the flux measurements for the used star. Nevertheless, since the standards and the target were observed at different sky positions, we also compared the magnitudes of several field stars with those from the Sloan Digital Sky Survey (SDSS) Release 14 catalogue (Abolfathi et al. 2018) and the Pan-STARRS catalogue (Flewelling et al. 2020). To convert the Pan-STARRS magnitudes to the SDSS photometric system, we used equation (6) from Tonry et al. (2012). The stars used in this analysis are shown in Fig. 1 and listed in Table 2. Their catalogue g'-band magnitudes were found to be consistent within uncertainties with those calibrated using the photometric standard. However, in case of the r' and i' bands, we found a slight discrepancy between the respective magnitudes. In addition, we calculated the colour term corrections and found that they are negligible in the r' and i' bands, and only slightly affect the g'-band measurements. Accounting for all of the mentioned corrections, the resulting zero points are $Z_{g'} = 28.51(2)$, $Z_{r'} = 29.03(3)$, and $Z_{i'} = 28.34(3)$. The point source 3σ upper limits in individual $g'r'i'$ exposures are $g' = 26.4$, $r' = 25.8$, and $i' = 24.8$. We note that all magnitudes presented in this paper are in the AB system.

2.2 Radio data

J1641 is being observed by the CHIME telescope (CHIME; CHIME Collaboration 2022). For this work, we processed and analysed high-cadence timing data recorded with the pulsar-timing backend built for CHIME (CHIME/Pulsar Collaboration 2021). The CHIME/Pulsar backend generates folded profiles evaluated over 10-s integrations and 1024 frequency channels that span the 400–800 MHz range. These data are coherently dedispersed in real time and prior to folding, using the value of DM listed in Table 3.

The CHIME/Pulsar data set on J1641 currently spans ∼3 yr of observations between early 2020 and 2023, and is being collected in support of ongoing GBNCC analyses (McEwen et al., in preparation). All data were processed – through statistical cleaning of radio-frequency interference and downsampling to 32 channels – using the PSRCHIVE (van Straten, Demorest & Oslowski 2012) and CLFD (Morello et al. 2019) analysis suites. Once initially cleaned, a subset of data was co-added to form a high-significance pulse profile that turned into a 'standard template' after de-noising; this standard template was then used to compute times of arrival (TOAs) for the entire CHIME/Pulsar data set, yielding 32 TOAs per epoch that are each evaluated across 32 downsampled frequency channels. Any TOAs with S/N values less than 8.0, as determined with the PAT utility in PSRCHIVE, were excluded from analysis based on sub-optimal detection statistics. For the remaining data set, a small, additional amount of TOAs ($\ll$1 per cent) were excised during the timing analysis due to corruption of the pulse profile from sub-threshold interference that was not detected during the data-preparation process.

2.3 X-ray data

The J1641 field was observed in the course of SRG/*eROSITA* all-sky survey in four visits spanning between 2020 April 9 and 2021 October 13 with the total exposure time of 2.8 ks. No source was statistically significantly detected at the pulsar position. The derived upper limit on the unabsorbed flux is $\approx 1.3 \times 10^{-14}$ erg s^{-1} cm^{-2} in the 0.5–10 keV range (90 per cent confidence), assuming a power law (PL) model with the photon index $\Gamma = 2.5$ (the average value for BWs, Swihart et al. 2022) and the absorbing column density $N_{\rm H} = 7 \times 10^{20}$ cm^{-2}. The latter was derived using the reddening $E(B-V) = 0.08$ mag obtained for J1641 from the extinction map of Green et al. (2019) and the empirical relation from Foight et al. (2016). Note that the reddening is equal to that obtained from the optical light-curve modelling (see below).

3 UPDATED RADIO TIMING OF PSR J1641+8049

We refined the timing model of J1641, based on the solution developed by Lynch et al. (2018), using the TEMPO pulsar-timing package to obtain updated estimates of the spin, astrometric, and orbital parameters based on the CHIME/Pulsar data set alone. We also incorporated 355 additional degrees of freedom to fit for DM in contiguous time bins of 1.5-d extent that span the timespan of the data set. Due to the turbulent environments often observed in BW systems, we also explored the fitting of parameters that quantify variations in the orbital elements.

A summary of the best-fitting CHIME/Pulsar timing residuals for J1641 and DM timeseries is shown in Fig. 2, and timing model parameters are reported in Table 3. One important result from our updated modelling is that the CHIME/Pulsar data yielded statistically different estimates of the proper motion than those obtained by Lynch et al. (2018), with the new magnitude of proper motion $\mu = 2.02(10)$ mas yr^{-1} being lower by a factor of ∼20. We attribute this difference to the high-cadence nature of the CHIME/Pulsar TOAs, which allow for better estimates of short-term variations that are typically observed in other BW systems. This change in proper motion mainly impacts the derived estimate of 'intrinsic' spin-down of the pulsar, i.e. the time rate of change in spin frequency corrected for biases induced by proper motion and acceleration in the Galactic potential (e.g. Nice & Taylor 1995). The corrected spin-down we

Table 3. The J1641 parameters derived from observations with the CHIME/Pulsar backend.

Logistics of CHIME/Pulsar radio observations	
MJD range of observations, MJD	59030–60063
Frequency range, MHz	400–800
Number of channelized TOAs per epoch	32 (maximum)
Number of observing epochs	581
Number of TOAs, total	7793
TEMPO goodness-of-fit (χ^2) statistic	9970
TEMPO reduced χ^2 statistic	1.04
TEMPO root-mean-square residual, μs	1.88
TEMPO scaling factor for raw uncertainties	1.7
Best-fitting timing parameters from TEMPO	
Right ascension (J2000), hh:mm:ss	16:41:20.83311(3)
Declination (J2000), dd:mm:ss	80:49:52.92335(8)
Proper motion in RA, mas yr^{-1}	$-1.74(10)$
Proper motion in Dec., mas yr^{-1}	$-1.03(11)$
Timing parallax, mas	$-4(4)$
Spin frequency f, Hz	494.760636473171(4)
Time derivative in spin frequency, Hz^2	$-2.3928(2) \times 10^{-19}$
Epoch of reference for pulsar spin, MJD	59315.1255
DM used for observations, pc cm^{-3}	31.091883
Best-fitting DMs, binned	see Section 3
Binary model used by TEMPO	ELL1
Projected semimajor axis, lt-s	0.06407531(17)
Epoch of passage through asc.-node longitude, MJD	59315.04093360(5)
ELL1 eccentricity parameter #1	0.000019(4)
ELL1 eccentricity parameter #2	$-0.000010(4)$
Orbital frequency n_b, Hz	$1.2736404201(2) \times 10^{-4}$
First time-derivative in n_b, Hz^2	$-9.9(3) \times 10^{-20}$
Second time-derivative in n_b, Hz^3	$-1.89(16) \times 10^{-27}$
Derived parameters from CHIME/Pulsar radio observations	
Proper motion μ, mas yr^{-1}	2.02(10)
Observed spin-period derivative $\dot{P}$, s s^{-1}	$9.7748(9) \times 10^{-21}$
Intrinsic spin-period derivative $\dot{P}_i$, s s^{-1}	$10.169(12) \times 10^{-21}$
Mass function f_M, M$_\odot$	3.42×10^{-5}
Characteristic age $\tau_c \equiv P/2\dot{P}$, Gyr	3.28
Observed spin-down luminosity $\dot{E}$, erg s^{-1}	4.67×10^{34}
Intrinsic spin-down luminosity $\dot{E}_i$, erg s^{-1}	4.86×10^{34}
Magnetic field at the equator $B_{\rm eq}$, G	1.42×10^8

Notes. Numbers in parentheses denote 1σ uncertainties relating to the last significant digit quoted.
Spin-down luminosities are calculated assuming the canonical moment of inertia of 10^{45} g cm^2.
$\dot{E}_i$ is calculated based on the distance $D = 4.6(2)$ kpc derived from our modelling (see text).

derive for J1641 is discussed in Section 5 as it depends on results obtained from the optical analysis presented below.

Our timing model of orbital motion uses the ELL1 formalism to describe low-eccentricity orbits (Lange et al. 2001). The best-fitting ELL1 model indicates that deviations from purely Keplerian motion are detectable in the CHIME/Pulsar data set. The inclusion of one time derivative in orbital frequency $n_b = 2\pi/P_b$ as a degree of freedom improves the fit of the timing model by an amount $\Delta\chi^2 \approx 17\,000$. We found that fitting for two time-derivatives in n_b, along with the five Keplerian elements, yielded an optimal fit to the timing data. The interpretation of these parameters in terms of macroscopic quantities (e.g. mass and/or geometry) is non-trivial due to the complex environment in BW systems that produce stochastic orbital variations (e.g. Shaifullah et al. 2016). Future analysis of orbital evolution in the J1641 system will be performed once several years of additional CHIME/Pulsar data are obtained.

The reliable detection of J1641 indicates minimal eclipsing of radio signal at superior conjunction. However, the DM variations in Fig. 2 show secular and quasi-periodic trends over time. The estimate of μ for J1641 none the less remains comparable whether we use a many-bin DM model or a polynomial expansion in DM, which differ in functional form and by hundreds of fit parameters. This circumstance indicates that proper motion is robustly measured with the CHIME/Pulsar data set despite only spanning ~3 yr in time and regardless of the choice in DM model.

In order to better assess these variations, we generated a separate timing solution based on data acquired in the MJD 59000–59400 range[5] and setting maximum DM-bin extents to be 0.5 d, i.e. to ensure a single DM is estimated for each observing epoch. Despite the shortened data set, we fit for the same parameters reported in Table 3 in order to separately measure variations in celestial position, DM, and orbital motion.

The results of this data-subset modelling is shown in Fig. 3, which shows this residual subset as function of time and orbital phase. In the

[5]While arbitrary, this range was chosen since the default version of TEMPO is unable to accommodate the total number of per-epoch DM parameters needed to model the entire CHIME data set.

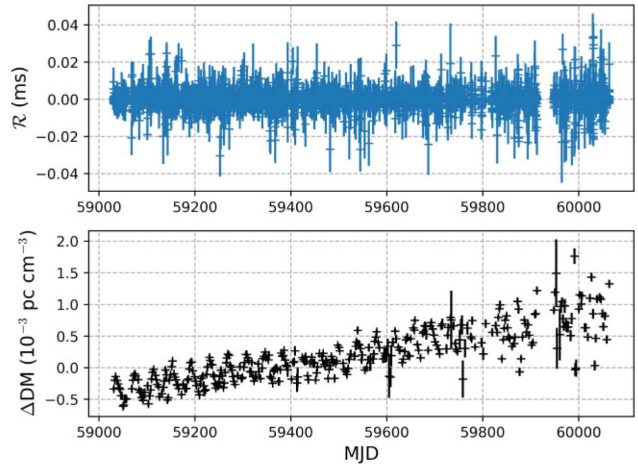

Figure 2. Best-fitting timing residuals ($\mathcal{R}$, top) and DM values determined for the CHIME/Pulsar data set described in Section 2.2. The DM values are plotted as changes relative to the value reported in Table 3.

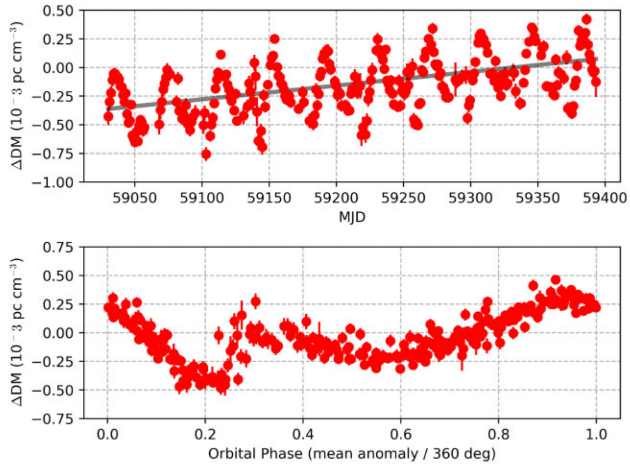

Figure 3. Per-epoch measurements of DM for J1641 plotted as a function of time (top) and orbital phase (bottom), estimated by fitting to all CHIME/Pulsar data within the MJD 59000–59400 range. In the top panel, the line is a best-fitting estimate of the secular variation over time that is presumed to be linear. In the bottom panel, the DM values have been corrected for the secular variation.

ELL1 binary model, the orbital phase $\Phi = n_b(t - T_{\rm asc})/(2\pi)$, where $T_{\rm asc}$ is the epoch of passage through the longitude of ascending node specified in Table 3; superior conjunction corresponds to $\Phi = 0.25$ in Fig. 3. The fitting of per-epoch DMs allows for better resolution of periodic variations, though requires at least 270 DM-bin fit parameters for the MJD 59000–59400 portion of the data alone. None the less, the per-epoch DMs exhibit clear periodic variations that occur on a time-scale equal to the orbital period for J1641; the ~monthly variation in the DM timeseries is a manifestation of aliasing due to CHIME/Pulsar observations occuring once every sidereal day. While an excess in DM coincides with superior conjunction, the DM appears to modulate over the whole orbit and thus indicates a structured circumbinary medium. Further analysis of the DM variations over the entirety of the J1641 data set, as well as other BW systems discovered and monitored by GBNCC, will be presented in future work.

4 PSR J1641+8049 OPTICAL LIGHT CURVES AND THE SYSTEM PARAMETERS

The resulting g', r', i'-band light curves folded with the orbital period are presented in Fig. 4, left. In the right panel of Fig. 4, we show the HiPERCAM data obtained in the u_s', g_s', r_s', i_s', and z_s' bands about 1 yr before our observations (Mata Sánchez et al. 2023). The shapes of the light curves are found to be consistent, nevertheless the object appears to be slightly brighter and bluer at the maximum of the light curves in the HiPERCAM data. To demonstrate this, in Fig. 5 we present the source broad-band optical spectra in the maximum of the light curves, corresponding to the OSIRIS (blue) and the HiPERCAM (green) data. The slopes[6] of the spectra $F \sim \lambda^{\alpha}$ are $\alpha_{\rm OSIRIS} = -1.74(21)$ and $\alpha_{\rm HiPERCAM} = -2.01(18)$, respectively. As it can be seen, there is a brightness-decreasing tendency together with a relative reddening of the object spectrum on the time-scale of these observations. We also note that the flux measurements close to the photometric maximum obtained with the McDonald Observatory 1 m telescope were brighter than those reported for the GTC/HiPERCAM observations, whereas the LDT measurements were mostly close to them (Lynch et al. 2018; D. Kaplan, private communication). For comparison, in Fig. 6 we show the r'-band light curves with all available data points.

To estimate the system parameters, we fitted the light curves using the emission model of a binary system described in Zharikov et al. (2013, 2019). The model consists of an NS as the primary that heats a low-mass companion as the secondary. The spectrum of each surface element of the companion is approximated by a blackbody with an effective temperature that is distributed non-uniformly over the star surface accounting for its heating by the pulsar. The contribution of the pulsar into the observed optical flux is negligible for any expected distance and NS brightness values. Following Zharikov et al. (2019), the effective irradiation factor of the secondary is related to the heating efficiency η and the spin-down luminosity of the pulsar as

$$K_{\rm irr} = \frac{\eta \dot{E}_i}{4\pi^2 R_{\rm NS}^2}, \tag{1}$$

and it defines the effective radiate flux $F_{\rm in}$ transferred from the pulsar to the secondary:

$$F_{\rm in} = \cos(\alpha_{\rm norm})\Omega \Delta S K_{\rm irr}, \tag{2}$$

where $\alpha_{\rm norm}$ is the angle between the incoming flux and the normal to the surface, $\Omega = \pi R_{\rm NS}^2/a^2$ is the solid angle from which the pulsar is visible from the surface element ΔS of the companion, $R_{\rm NS} = 13$ km is the NS radius, and a is the orbit separation. The corresponding 'day-side' temperature of the companion star surface element is

$$T_{\rm d} = T_{\rm n}\left[1 + \frac{F_{\rm in}}{\sigma \Delta S (T_{\rm n})^4}\right]^{1/4}, \tag{3}$$

where σ is the Stefan–Boltzmann constant. The phase-resolved light curves were calculated by integrating the flux from all visible elements of the secondary in the corresponding band. The gradient descent method was used to find the minimum of χ^2 defined as

$$\chi^2 = \sum_j^{g',r',i'} \sum_k^{N_j} \left(\frac{O_k - C_k}{\sigma_k}\right)^2, \tag{4}$$

where N_j is the number of observations in a given filter, O_k, C_k, and σ_k are the observed and the calculated magnitudes, and the error of the observed magnitude, respectively. The free fitted parameters

[6]Without the u_s' band for the HiPERCAM data.

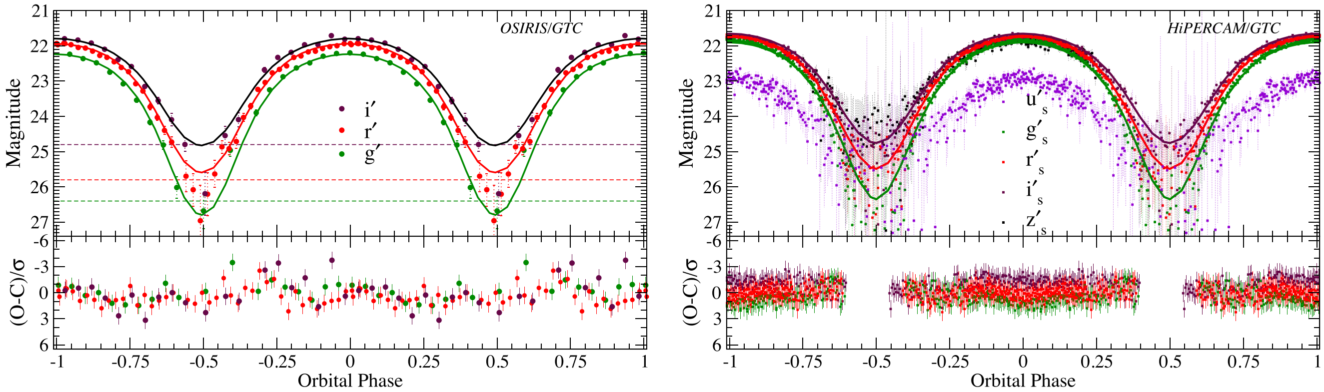

Figure 4. *Top-left*: Multicolour light curves of J1641 obtained with the OSIRIS/GTC (g', r', i') folded with the orbital period. The phase zero corresponds to the orbital phase when the companion day-side is facing an observer. Two orbital cycles are shown for clarity. Solid lines represent the result of the best fit of the data by the model where the companion is heated by the pulsar. Horizontal dashed lines show 3σ detection limits of the observations. *Top-right*: The HiPERCAM/GTC multiband data of J1641 and the best fit of the g_s', r_s', i_s' light curves by the model. *Bottom panels*: Fit residuals calculated as the difference between the observed (O) and the calculated (C) magnitudes for each data point in terms of the magnitude error σ.

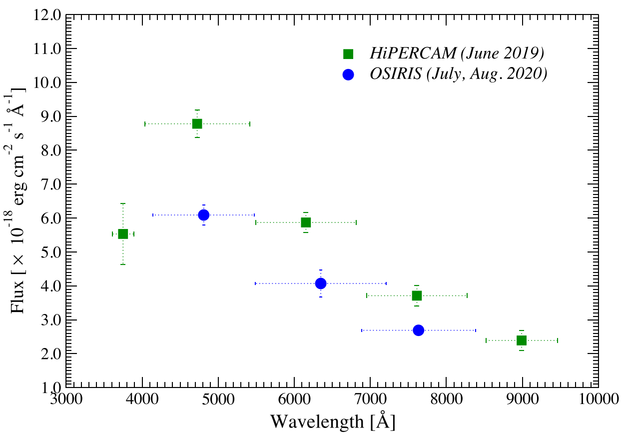

Figure 5. The broad-band optical spectra of the J1641 optical component at the photometric maximum for different epochs of observations.

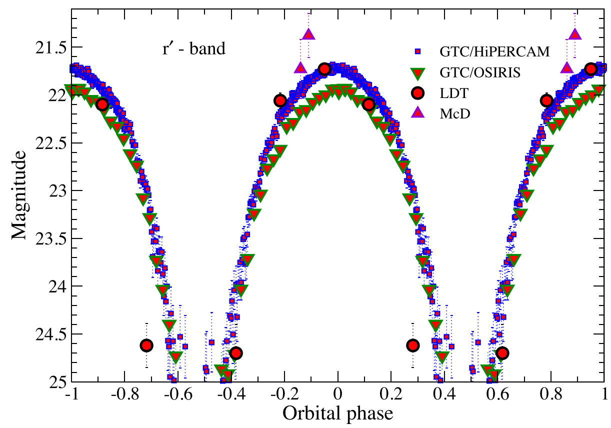

Figure 6. The r'-band light curves folded with the orbital period obtained with the GTC, LDT, and McD. The orbital phase $\phi = 0.0$ corresponds to the maximum of the GTC/HiPERCAM light curve and it is shifted to -0.76 from the radio convention orbital phase, where $\phi = 0.0$ corresponds to the ascending node. LDT and McDonald 1-m telescope data were obtained in 2017 March.

were the distance D, the reddening $E(B - V)$, the binary system inclination i, the Roche lobe filling factor f_x defined as a ratio of distances from the centre of mass of the secondary to the star surface and to the Lagrange point L_1, the 'night-side' temperature $T_{\rm n}$ of the secondary, the effective irradiation factor $K_{\rm irr}$ [ergs s^{-1} cm^{-2} sr^{-1}], the pulsar mass $M_{\rm NS}$, and the component mass ratio.

The best-fitting model light curves for the OSIRIS data are shown in the left panel of Fig. 4 by solid lines. The model parameters are given in the second column of Table 4. The uncertainty of each fitted parameter was calculated following the method proposed by Lampton, Margon & Bowyer (1976). The geometry of the system and the distribution of the effective temperature at the companion surface for the OSIRIS data are shown in Fig. 7. For comparison, we also used the model for the HiPERCAM g_s'-, r_s'-, i_s'-band light curves. We limited our analysis of the HiPERCAM data to the three close optical bands because a simple blackbody spectrum approximation for radiation from a star surface element used in the model cannot describe the companion spectrum in a wide spectral range from the u_s' up to the z_s' band. On the other hand, this approach was applied to simplify the comparison of the fit results achieved using the same model setup in both cases. Since the source was slightly brighter and bluer in the HiPERCAM data compared to the OSIRIS data, we first fixed all model parameters excluding the secondary heating at the values given in Table 4 for the OSIRIS data, and then fitted the HiPERCAM data. The fit provided a hotter day-side part of the secondary with a maximum temperature of about 9200 K. After that, we thawed all parameters as in the case of the OSIRIS data. The best-fitting parameters of the last fit are given in the third column of Table 4. In general, they are close to or inside the 1σ error range of the OSIRIS data fit results, except for the effective irradiation factor $K_{\rm irr}$, which, in turn, gives a higher day-side temperature of the secondary. Another difference is related to the mass of the pulsar. The fitting of the two data sets results in a significantly lower mass in the HiPERCAM data compared to that in the OSIRIS data. Nevertheless, their 1σ uncertainties overlap. We note that the light-curve shapes and fluxes are mainly defined by the size of the companion Roche lobe, its filling factor, temperature distribution, and system inclination. The Roche lobe size is changed by 15 per cent at the variation of the pulsar mass within its reasonable limits. To get the observed light curves, these changes can be compensated by variations of the temperature and filling factor. Thus, these parameters are correlated and additional information is needed to better constrain them.

For instance, we can utilize the mass function from the new radio timing measurements (see Table 3). It decreases the numbers of free parameters, because it links the pulsar mass, the inclination, and the mass of the companion. Taking into account the mass function we repeated the fitting of the data from both instruments. The results are presented in the last two columns of Table 4. They are very close to those obtained by Mata Sánchez et al. (2023) who used the ICARUS code (Breton et al. 2012) to model the HiPERCAM data (see table 3 in the respective paper). However, we note that the formal χ^2 values are higher as compared to the cases when the masses of components and inclination are free parameters. All results are summarized in Fig. 8 and discussed below.

5 DISCUSSION AND CONCLUSIONS

As it was mentioned before, the J1641 orbital period of 2.18 h is one of the shortest among the known BWs (Swihart et al. 2022), and its highly modulated optical light curves are typical for such tight binary systems with MSPs. The shapes of the light curves do not demonstrate significant changes on a 1-yr time-scale between the HiPERCAM and OSIRIS observations. However, the fluxes at the photometric maximum exhibit a significant decrease between the observations by up to a factor of two. This can indicate variability of the pulsar wind on a short (days) and long (years) time-scales. We note that variable heating (increases and decreases of the companion irradiation by the pulsar) is observed for some other MSP binary systems, such as, e.g. the BW candidate 4FGL J0935.3+0901 (Halpern 2022) or the redback PSRs J1048+2339 (Yap et al. 2019) and J2129-0429 (Bellm et al. 2016). Follow-up observations are needed to confirm and study this effect for J1641.

The previously reported proper motion $\mu = 39(3)$ mas yr^{-1} for J1641 led to a negative value of the pulsar intrinsic spin-down luminosity, implying a spin-up scenario (Lynch et al. 2018; Mata Sánchez et al. 2023), which could indicate the presence of accretion. However, the latter would complicate detection of radio pulsations from the pulsar and affect the optical light curves of the system. Neither the HiPERCAM nor the OSIRIS observations support this scenario. In addition, using the distance obtained through the HiPERCAM light-curve modelling, Mata Sánchez et al. (2023) concluded that the maximum proper motion for this system, which would allow to avoid the spin-up scenario, is $\mu \leq 19$ mas yr^{-1}. Indeed, the updated proper motion $\mu = 2.02(10)$ mas yr^{-1} derived from the new radio observations (see Section 2.2) is significantly lower than the one provided by Lynch et al. (2018). It yields a new estimation on the intrinsic period derivative, $\dot{P}_i$ and the intrinsic spin-down luminosity $\dot{E}_i$. Considering the distance $D = 4.6(2)$ kpc obtained from our optical light-curve modelling, we estimated the Shklovskii correction (Shklovskii 1970), $\dot{P}_{\rm Shk} \approx 0.08 \times 10^{-21}$ s s^{-1}. Taking into account the corrections due to the differential Galactic rotation and the pulsar acceleration, the corresponding intrinsic period derivative is $\dot{P}_i = 10.2 \times 10^{-21}$ s s^{-1}, and the spin-down luminosity is $\dot{E}_i = 4.87 \times 10^{34}$ erg s^{-1}, rejecting the spin-up and accretion scenario. We note that in the case of this particular BW system, the Shklovskii correction is subdominant leading to the fact that the intrinsic spin-down luminosity is ≈4 per cent higher than the observed one. In addition, taking into account the newly determined proper motion, we can now estimate the J1641 transverse velocity. Considering the distance 4.6 kpc derived from the light-curve modelling and following Verbunt, Igoshev & Cator (2017) to estimate the contribution of the Galactic rotation and solar peculiar velocity, we obtain $V_T \approx 36$ km s^{-1} in the local standard of rest of the pulsar. This velocity is typical for pulsar binary systems (Hobbs et al. 2005).

According to Mata Sánchez et al. (2023), J1641 has one of the heaviest companions ($M_{\rm c} = 0.055^{+0.016}_{-0.014}$ M$_\odot$) among the known BWs. More massive secondaries were found for, e.g. PSR J1555−2908 ($0.060^{+0.005}_{-0.003}$ M$_\odot$; Kennedy et al. 2022) and PSR J1810+1744 (0.065(1) M$_\odot$; Romani et al. 2021). However, our fit for all free parameters resulted in a lower companion mass of 0.035(13) M$_\odot$ and 0.025(4) M$_\odot$ for the OSIRIS and HiPERCAM data, respectively. These values are close to the average mass $\bar{m}_c = 0.026(15)$ of pulsar companions in BW systems (Swihart et al. 2022, see table 5 therein). However, the value for the HiPERCAM fit is inconsistent with the mass function derived from the radio timing (see Fig. 8), while the value for the OSIRIS fit agrees with it. Taking the mass function into account we got the mass of the companion of 0.046(10) M$_\odot$ for both data sets. This is in agreement with the values reported by Mata Sánchez et al. (2023). Thus, the companion indeed can be rather heavy in comparison with other BW systems.

Another distinct feature of J1641 is the high day-side temperature of the companion, 8200–9500 K, making it one of the five most heated sources among the known BWs (see Fig. 9). The other four sources are PSR J1311−3430 with $T_{\rm d} \gtrsim 12\,000$ K (Romani et al. 2012; Romani, Filippenko & Cenko 2015), the BW candidate ZTF J1406+1222 with $T_{\rm d} \approx 10\,500$ K (Burdge et al. 2022), PSR J1810+1744 with $T_{\rm d} \approx 9400$ K (Romani et al. 2021) and PSR J1555−2908 with $T_{\rm d} \approx 9400$ K (Kennedy et al. 2022). The J1641 day-side temperature is ≳2 times larger than the respective temperatures of, e.g. PSR J0251+2606 (≈3400 K) or PSR J0636+5129 (≈4600 K) (Mata Sánchez et al. 2023) near the low end of the source temperature distribution. It seems natural that the number of companions with a lower day-side temperature is larger than that with a hotter one, as the latter have to be evaporated faster. However, it remains unclear how the companion heating is related to the 'spin-down flux' defined as $\dot{E} P_b^{-4/3}$ (Zharikov et al. 2019, see fig. 5 and table 5 therein). It is possible that the absence of a clear dependence on the spin-down luminosity and/or system separation indicates the importance of the pulsar wind instability and/or asymmetry in the companion heating.

Using the intrinsic spin-down luminosity $\dot{E}_i$ and the irradiation factor $K_{\rm irr}$, we estimated the irradiation efficiency range $\eta \approx 0.3$–0.7. These values seem to overshoot those typically observed for BWs (e.g. Draghis et al. 2019). An irradiation luminosity even larger than $\dot{E}$ ($\eta \gtrsim 1$), calculated assuming a canonical momentum of inertia value of 10^{45} g cm^2, was derived, e.g. for BW PSR J1810+1744 by Romani et al. (2021). It is also an additional argument that the true one can be lower due to the beaming factor (see Draghis et al. 2019; Romani et al. 2021).

The derived companion mass of J1641 (Table 4) is close to typical masses of brown dwarfs (0.01–0.07 M$_\odot$) implying the possible origin of the companion. However, a field brown dwarf with an age of ≳ 1 Gyr, similar to the J1641 characteristic age (Table 3), would be twice more compact (≲0.1 R$_\odot$) and colder (≲ 1500 K; Marley et al. 2021) as compared to the derived night-side temperature of J1641. This disfavours the brown dwarf nature of the companion. Nevertheless, such a discrepancy appears to be not a unique property of J1641. As was noted before, most BW companions, especially the strongly heated, are bloated up by a factor of two in comparison with the Galactic field brown dwarfs (Kandel & Romani 2023, see table 6 therein). The strong irradiation by the pulsar can affect the global

Table 4. The light-curve fitting results for J1641.

Mass function $\times 10^{-5}$, $M_\odot$ (fixed)	–	–	3.42	3.42
Fitted parameters	OSIRIS	HiPERCAM	OSIRIS	HiPERCAM
Pulsar mass M_{NS}, $M_\odot$	2.0(6)	1.3(4)	1.3(3)	1.3(1)
Mass ratio $q = M_c/M_{NS}$	0.018(4)	0.019(2)	0.035	0.036
Distance D, kpc	4.60(20)	4.70(20)	4.64(12)	4.83(13)
Reddening $E(B-V)$, mag	0.072(23)	0.056(30)	0.09(2)	0.07(3)
'Night-side' temperature T_n, K	3300(100)	3400^{+400}_{-300}	3380(120)	3500^{+300}_{-180}
Inclination i, deg	57(7)	56(10)	59(8)	58(10)
Roche lobe filling factor f_x	$0.95^{+0.05}_{-0.10}$	$0.90^{+0.10}_{-0.09}$	$0.99^{+0.01}_{-0.08}$	$0.87^{+0.13}_{-0.07}$
Irradiation factor K_{irr}, $\times 10^{20}$ erg cm^{-2} s^{-1} sr^{-1}	4.3(3)	5.8(5)	1.9(1)	3.6(2)
χ^2/d.o.f.	138/73	767/956	167/74	2525/957
Derived parameters				
Companion mass M_c, $M_\odot$	0.038	0.025	0.046	0.047
Companion radius $R_{c,x}$, $R_\odot$	0.194	0.165	0.220	0.198
Companion radius $R_{c,y}$, $R_\odot$	0.143	0.121	0.167	0.144
Lowest 'day-side' temperature T_d^{min}, K	3800	4250	3940	4410
Highest 'day-side' temperature T_d^{max}, K	8200	9500	8000	8700
Irradiation efficiency η	0.45	0.7	0.3	0.5

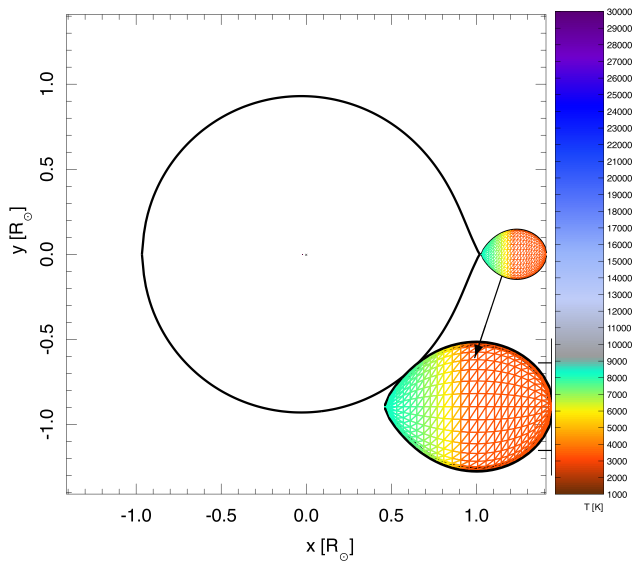

Figure 7. The Roche lobe of the system components and a magnification of the secondary. The gradient shows the effective temperature distribution on the secondary surface. The image corresponds to the OSIRIS data modelling, when all parameters are free.

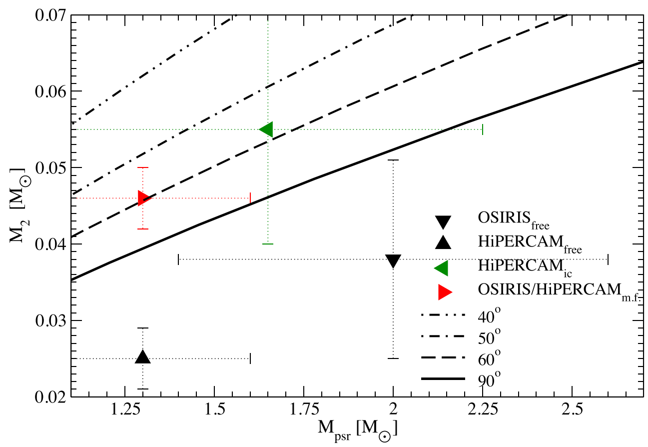

Figure 8. The masses of the pulsar and its companion from the fits of the optical light curves. The lines show the relation between masses at different orbit inclinations based on the mass function found from the pulsar radio timing. The triangles labelled as OSIRIS$_{free}$ and HiPERCAM$_{free}$ correspond to the fits when the masses and inclinations are free parameters. The triangle labelled as OSIRIS/HiPERCAM$_{m.f.}$ marks the fits that take into account the mass function. The triangle marked as HiPERCAM$_{ic}$ shows the result from Mata Sánchez et al. (2023).

structure of the presumed brown dwarf leading to the increase of its night-side temperature as well.

Finally, J1641 is not detected in X-rays in the 2.8 ks data accumulated during the SRG/*eROSITA* all-sky survey. The upper limit (90 per cent) on its X-ray luminosity is about 3.3×10^{31} erg s^{-1} for a distance of 4.6 kpc. This and the γ-ray luminosity 5×10^{33} erg s^{-1} (Swihart et al. 2022) are typical for BWs.

In addition to follow-up optical broad-band observations to confirm the optical variability of the companion, optical spectroscopy would be useful to establish its spectral type and to measure its radial velocity curve, to better constrain the parameters of the system.

ACKNOWLEDGEMENTS

We thank the referee for their useful comments and suggestions that allowed us to improve the manuscript. We also thank Daniel Mata Sanchez and David Kaplan for providing the optical data and for useful discussions, and Andrei Igoshev for his helpful comments. The work is based on observations made with the Gran Telescopio Canarias (GTC), installed at the Spanish Observatorio del Roque de los Muchachos of the Instituto de Astrofísica de Canarias, on the island of La Palma. This work used data obtained with eROSITA telescope onboard SRG observatory. The SRG observatory was built by Roskosmos in the interests of the Russian Academy of Sciences represented by its Space Research Institute (IKI) in the framework of the Russian Federal Space Program, with the participation of the Deutsches Zentrum für Luft- und Raumfahrt (DLR). The SRG/eROSITA X-ray telescope was built by a consortium of German

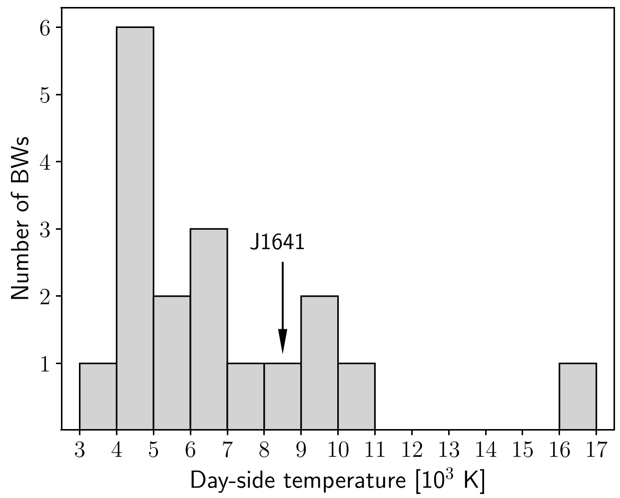

Figure 9. Distribution of the day-side temperature $T_{\rm d}$ of BW companions. 18 sources are included. For PSRs J0023+0923, J0251+2606, J0636+5129, J0952−0607, J1124−3653, J1301+0833, J1544+4937, J1555−2908, J1653−0158, J1810+1744, J1959+2048, J2051−0827, J2052+1219, J2241−5236, and J2256−1024, the day-side temperatures are calculated using the base (night-side) and the irradiation temperatures ($T_{\rm n}$ and $T_{\rm irr}$) from Mata Sánchez et al. (2023) (see their table A1 and references therein). For PSR J1311−3430, Kandel & Romani (2023) obtained very low $T_{\rm n}$, negligible in comparison with $T_{\rm irr}$, which was derived from the irradiation luminosity and parameters of the orbit (i.e. $T_{\rm d} \approx T_{\rm irr}$). The position of J1641 according to our fit of the OSIRIS data is marked by the arrow. We also include the BW candidate ZTF J1406+1222 (Burdge et al. 2022). The best-fitting value of the base temperature of PSR J0610−2100 is below the lowest temperature covered by the spectral models (van der Wateren et al. 2022); thus, we excluded it from the sample.

Institutes led by MPE, and supported by DLR. The SRG spacecraft was designed, built, launched and is operated by the Lavochkin Association and its subcontractors. The science data are downlinked via the Deep Space Network Antennae in Bear Lakes, Ussurijsk, and Baykonur, funded by Roskosmos. The eROSITA data used in this work were processed using the eSASS software system developed by the German eROSITA consortium and proprietary data reduction and analysis software developed by the Russian eROSITA Consortium. We acknowledge that CHIME is located on the traditional, ancestral, and unceded territory of the Syilx/Okanagan people. We are grateful to the staff of the Dominion Radio Astrophysical Observatory, which is operated by the National Research Council of Canada. CHIME is funded by a grant from the Canada Foundation for Innovation (CFI) 2012 Leading Edge Fund (Project 31170) and by contributions from the provinces of British Columbia, Québec, and Ontario. The CHIME/FRB project is funded by a grant from the CFI 2015 Innovation Fund (Project 33213) and by contributions from the provinces of British Columbia and Québec, and by the Dunlap Institute for Astronomy and Astrophysics at the University of Toronto. Additional support is provided by the Canadian Institute for Advanced Research (CIFAR), McGill University and the McGill Space Institute thanks to the Trottier Family Foundation, and the University of British Columbia (UBC). The CHIME/Pulsar instrument hardware is funded by the Natural Sciences and Engineering Research Council (NSERC) Research Tools and Instruments (RTI-1) grant EQPEQ 458893–2014. The work of DAZ and AVK was supported by the Russian Science Foundation, grant number 22-22-00921, https://rscf.ru/project/22-22-00921/. DAZ thanks Pirinem School of Theoretical Physics for hospitality. SVZ acknowledges PAPIIT grant IN119323. Pulsar research at UBC is funded by an NSERC Discovery Grant and by the Canadian Institute for Advanced Research. FAD is supported by the UBC Four Year Fellowship. MAM is supported by the NANOGrav NSF Physics Frontiers Center award numbers 1430284 and 2020265 and NSF award number 2009425. JKS is supported by the NANOGrav NSF Physics Frontiers Center award numbers 1430284 and 2020265. This work has made use of data from the European Space Agency (ESA) mission *Gaia* (https://www.cosmos.esa.int/gaia), processed by the *Gaia* Data Processing and Analysis Consortium (DPAC, https://www.cosmos.esa.int/web/gaia/dpac/consortium). Funding for the DPAC has been provided by national institutions, in particular the institutions participating in the *Gaia* Multilateral Agreement. The Pan-STARRS1 Surveys (PS1) and the PS1 public science archive have been made possible through contributions by the Institute for Astronomy, the University of Hawaii, the Pan-STARRS Project Office, the Max-Planck Society and its participating institutes, the Max Planck Institute for Astronomy, Heidelberg and the Max Planck Institute for Extraterrestrial Physics, Garching, The Johns Hopkins University, Durham University, the University of Edinburgh, the Queen's University Belfast, the Harvard-Smithsonian Center for Astrophysics, the Las Cumbres Observatory Global Telescope Network Incorporated, the National Central University of Taiwan, the Space Telescope Science Institute, the National Aeronautics and Space Administration under grant no. NNX08AR22G issued through the Planetary Science Division of the NASA Science Mission Directorate, the National Science Foundation grant no. AST-1238877, the University of Maryland, Eotvos Lorand University (ELTE), the Los Alamos National Laboratory, and the Gordon and Betty Moore Foundation.

DATA AVAILABILITY

The optical data are available through the GTC data archive: https://gtc.sdc.cab.inta-csic.es/gtc/, the CHIME data, and the *eROSITA* data – upon request.

REFERENCES

Abdollahi S. et al., 2022, ApJS, 260, 53
Ablimit I., 2019, ApJ, 881, 72
Abolfathi B. et al., 2018, ApJS, 235, 42
Alpar M. A., Cheng A. F., Ruderman M. A., Shaham J., 1982, Nature, 300, 728
Bellm E. C. et al., 2016, ApJ, 816, 74
Benvenuto O. G., De Vito M. A., Horvath J. E., 2014, ApJ, 786, L7
Benvenuto O. G., De Vito M. A., Horvath J. E., 2015, MNRAS, 449, 4184
Bisnovatyi-Kogan G. S., Komberg B. V., 1974, SvA, 18, 217
Breton R. P., Rappaport S. A., van Kerkwijk M. H., Carter J. A., 2012, ApJ, 748, 115
Burdge K. B. et al., 2022, Nature, 605, 41
CHIME Collaboration, 2022, ApJS, 261, 29
CHIME/Pulsar Collaboration, 2021, ApJS, 255, 5
Cabrera-Lavers A., Pérez-García A., Abril Abril M., Bongiovanni A., Cepa G., 2014, Canarian Observatories Updates CUps, Vol. 3, https://www.gtc.iac.es/instruments/osiris/media/CUPS_BBpaper.pdf
Chen H.-L., Chen X., Tauris T. M., Han Z., 2013, ApJ, 775, 27
Cordes J. M., Lazio T. J. W., 2002, preprint (astro-ph/0207156)
Draghis P., Romani R. W., Filippenko A. V., Brink T. G., Zheng W., Halpern J. P., Camilo F., 2019, ApJ, 883, 108
Flewelling H. A. et al., 2020, ApJS, 251, 7
Foight D. R., Güver T., Özel F., Slane P. O., 2016, ApJ, 826, 66
Gaia Collaboration, 2023, A&A, 674, A1

Ginzburg S., Quataert E., 2021, MNRAS, 500, 1592
Green G. M., Schlafly E., Zucker C., Speagle J. S., Finkbeiner D., 2019, ApJ, 887, 93
Guo Y., Wang B., Han Z., 2022, MNRAS, 515, 2725
Halpern J. P., 2022, ApJ, 932, L8
Hobbs G., Lorimer D. R., Lyne A. G., Kramer M., 2005, MNRAS, 360, 974
Kandel D., Romani R. W., 2023, ApJ, 942, 6
Kennedy M. R. et al., 2022, MNRAS, 512, 3001
Lampton M., Margon B., Bowyer S., 1976, ApJ, 208, 177
Lange C., Camilo F., Wex N., Kramer M., Backer D. C., Lyne A. G., Doroshenko O., 2001, MNRAS, 326, 274
Lynch R. S. et al., 2018, ApJ, 859, 93
Manchester R. N., 2017, J. Astrophys. Astron., 38, 42
Manchester R. N., Hobbs G. B., Teoh A., Hobbs M., 2005, AJ, 129, 1993
Marley M. S. et al., 2021, ApJ, 920, 85
Mata Sánchez D. et al., 2023, MNRAS, 520, 2217
Morello V. et al., 2019, MNRAS, 483, 3673
Nice D. J., Taylor J. H., 1995, ApJ, 441, 429
Predehl P. et al., 2021, A&A, 647, A1
Ray P., 2023, Public List of LAT-Detected Gamma-Ray Pulsars, https://confluence.slac.stanford.edu/display/GLAMCOG/Public+List+of+LAT-Detected+Gamma-Ray + Pulsars, (accessed September 28, 2023)
Romani R. W., Filippenko A. V., Silverman J. M., Cenko S. B., Greiner J., Rau A., Elliott J., Pletsch H. J., 2012, ApJ, 760, L36
Romani R. W., Filippenko A. V., Cenko S. B., 2015, ApJ, 804, 115
Romani R. W., Kandel D., Filippenko A. V., Brink T. G., Zheng W., 2021, ApJ, 908, L46
Shaifullah G. et al., 2016, MNRAS, 462, 1029
Shklovskii I. S., 1970, SvA, 13, 562
Smith J. A. et al., 2002, AJ, 123, 2121
Stovall K. et al., 2014, ApJ, 791, 67
Sunyaev R. et al., 2021, A&A, 656, A132
Swihart S. J., Strader J., Chomiuk L., Aydi E., Sokolovsky K. V., Ray P. S., Kerr M., 2022, ApJ, 941, 199
Tonry J. L. et al., 2012, ApJ, 750, 99
van der Wateren E. et al., 2022, A&A, 661, A57
van Dokkum P. G., 2001, PASP, 113, 1420
van Straten W., Demorest P., Oslowski S., 2012, Astron. Res. Technol., 9, 237
Verbunt F., Igoshev A., Cator E., 2017, A&A, 608, A57
Yao J. M., Manchester R. N., Wang N., 2017, ApJ, 835, 29
Yap Y. X., Li K. L., Kong A. K. H., Takata J., Lee J., Hui C. Y., 2019, A&A, 621, L9
Zharikov S., Tovmassian G., Aviles A., Michel R., Gonzalez-Buitrago D., García-Díaz M. T., 2013, A&A, 549, A77
Zharikov S., Kirichenko A., Zyuzin D., Shibanov Y., Deneva J. S., 2019, MNRAS, 489, 5547

This paper has been typeset from a TEX/LATEX file prepared by the author.